Soft Matter

PAPER

View Article Online
View Journal | View Issue

Cite this: *Soft Matter*, 2023, **19**, 4579

Comparative study of the self-assembly behaviour of 3-chloro-4-hydroxy-phenylazo dyes†

Wenke Müller, *[a] Ralf Schweins, [a] Bernd Nöcker,[b] Hans Egold[c] and Klaus Huber [c]

Received 14th April 2023,
Accepted 6th June 2023

DOI: 10.1039/d3sm00500c

rsc.li/soft-matter-journal

The complexity of intermolecular interactions and the difficulty to predict assembly behaviour solely based on chemical constitution was demonstrated by studying the self-assembly of three one-fold negatively charged 3-chloro-4-hydroxy-phenylazo dyes (Yellow, Blue and Red). Dye self-assembly was investigated using UV/vis- and NMR-spectroscopy, light- and small-angle neutron scattering. Significant differences between the three dyes were observed. While Yellow does not self-assemble, Red assembles into higher-order aggregates and Blue forms well-defined H-aggregate dimers with a dimerization constant of K_D = (728 ± 8) L mol^{-1}. Differences between dyes were suggested to emerge from variations in the propensity to form π–π-interactions due to electrostatic repulsion, sterical constraints and hydrogen-bonding interactions.

Introduction

Dye molecules have been subject to scientific investigations for decades in order to respond to the needs from industries in the field of textile- or paper dyeing. The replacement of natural dyes by synthetic dyes permitted the fine–tuning of dye properties by variation of chemical functionalities.[1–3] Apart from traditional dye research, the use of dyes as functional materials, *e.g.* in dye-sensitized solar cells or organic light-emitting diodes (OLEDs), has received increasing attention over the past 20 years.[4–6] Contrary to traditional dye research, where it often sufficed to consider molecular structure – molecular property relationships, the design of functional materials requires understanding dye–dye intermolecular interactions, which impacts properties such as absorption, solid-state fluorescence and electron transport in the solid state material.[4,7]

A possibility to reduce the complexity of a system whilst getting valuable insight into intermolecular interactions affecting the solid-state system is to consider the self-assembly of dye molecules in solution, as they constitute an intermediate between the monomeric dye and the solid-state material.[4,7] Furthermore, the investigation of dye self-assembly in solution may be helpful to understand and mimic biological systems within which dye molecules assemble to fulfil specific tasks like the assembly of chlorophylls in photosynthetic organisms.[4,8–11]

π–π-interactions are considered as one of the major driving forces for dye self-aggregation in solution.[12] Depending on chemical constitution of the dye and geometrical constraints, other intermolecular interactions such as Coulomb forces, hydrophobic effect and dispersion forces or hydrogen bonding may additionally influence self-assembly.[13] Owing to the amount and complexity of possible intermolecular interactions, the prediction of dye self-assembly structure was reported to be difficult if no distinct dominant contribution exists.[12]

Herein we report investigations confirming the difficulty to predict dye self-assembly structure solely based on the chemical constitution of the dye. For this purpose, the self-assembly behaviour of three azo dyes with one congruent structural subunit (Fig. 1) is investigated by means of UV/vis-spectroscopy, scattering methods and NMR-spectroscopy. Self-assembly structures are elucidated and analogies and differences discussed.

Experimental

Chemicals and sample preparation

Three azo dyes Yellow (HC Yellow 16, ≥99%), Blue (HC Blue 18, ≥99.8%) and Red (HC Red 18, ≥99%) were provided by KAO GmbH, Germany. The buffer salts sodium carbonate Na_2CO_3 (≥99.8%) and sodium bicarbonate $NaHCO_3$ (≥99.7%) were obtained from Sigma Aldrich Chemie GmbH, Germany. MilliQ water was used to prepare the $NaHCO_3/Na_2CO_3$ buffer solutions (pH = 10.5, ionic strength $I \approx 0.25$ M) for UV/vis-spectroscopy and light scattering samples. D_2O was used to prepare the $NaHCO_3/Na_2CO_3$ buffer solutions (pD = 10.7, ionic strength $I \approx 0.25$ M) for NMR and small-angle neutron scattering samples.

[a] *Institut Laue-Langevin, DS/LSS, 71 Avenue des Martyrs, 38000 Grenoble, France. E-mail: we-mue@gmx.net*
[b] *KAO Germany GmbH, Pfungstädter Straße 98-100, 64297 Darmstadt, Germany*
[c] *Universität Paderborn, Warburger Straße 100, 33098 Paderborn, Germany*

† Electronic supplementary information (ESI) available. See DOI: https://doi.org/10.1039/d3sm00500c

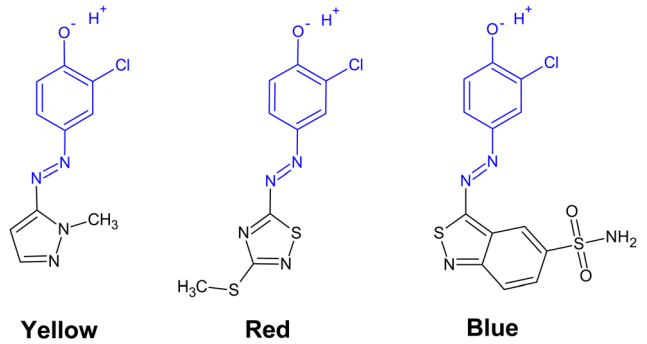

Fig. 1 Chemical structure of three azo dyes with their common structural sub-unit marked in blue. At alkaline pH such as pH = 10.5, the phenolate group is deprotonated in all cases.

D_2O (99.90% D) was obtained from Eurisotop, France. Chemicals were used without further purification. Samples were prepared from stock solutions, followed by a minimum equilibration time of 20 h at room temperature prior to analysis.

UV/vis spectroscopy

UV/vis spectra were recorded using a V-630 spectrometer from Jasco. Hellma quartz glass cuvettes with optical path lengths ranging from 0.01 cm to 1 cm were used for this purpose. The spectrometer was equipped with a thermostat to guarantee a constant measurement temperature of 25 °C.

Small-angle neutron scattering

Samples for small-angle neutron scattering (SANS) measurements were obtained by dissolving the respective dye in a $NaHCO_3$/Na_2CO_3 buffer in D_2O (pD = 10.7, ionic strength $I \approx 0.25$ M). The solution was subsequently filtered (MACHEREY-NAGEL, CHROMAFIL Xtra H-PTFE syringe filters, pore size 0.2 μm) into a dust-free sample vial and equilibrated for a minimum of 20 h at room temperature.

SANS was performed at the small-angle neutron scattering instrument D11 at the Institut Laue-Langevin (Grenoble, France). Different setups were used: (1) samples containing the dye Blue were measured at three sample-to-detector distances (28 m collimation 28 m), (8 m collimation 8 m), (1.7 m collimation 4.0 m) at a neutron wavelength of 6 Å to cover a q-range of 0.002 $Å^{-1}$ to 0.5 $Å^{-1}$. A circular neutron beam with a diameter of 15 mm was used. (2) The sample containing $[Red]_{tot}$ = 10 mM was measured at three sample-to-detector distances (38.0 m collimation 40.5 m), (10.5 m collimation 10.5 m), (1.7 m collimation 2.5 m) at a neutron wavelength of 6 Å to cover a q-range of 0.0014 $Å^{-1}$ to 0.5 $Å^{-1}$. A circular neutron beam with a diameter of 14 mm was used. (3) The sample containing $[Red]_{tot} \approx 5$ mM was measured at three sample-to-detector distances (38.0 m collimation 40.5 m), (10.5 m collimation 10.5 m), (2.5 m collimation 2.5 m) at a neutron wavelength of 6 Å to cover a q-range of 0.0014 $Å^{-1}$ to 0.5 $Å^{-1}$. A circular neutron beam with a diameter of 14 mm was used.

Neutrons were detected with a ^{3}He-detector (Reuter-Stokes multi-tube detector consisting of 256 tubes with a tube diameter of 8 mm and a pixel size of 8 mm × 4 mm), detector images azimuthally averaged, corrected to the transmission of the direct beam and scaled to absolute intensity using the Mantid software.[14,15] Solvent scattering and incoherent background were subtracted from the scattering curves.[16] SANS data were collected at a sample temperature of 25 °C.

NMR-spectroscopy

Samples for NMR-spectroscopy were obtained by dissolving the respective dye in a $NaHCO_3$/Na_2CO_3 buffer in D_2O (pD = 10.7, ionic strength $I \approx 0.25$ M). The solution was subsequently filtered (MACHEREY-NAGEL, CHROMAFIL Xtra H-PTFE syringe filters, pore size 0.2 μm) into the NMR-tube. ^{1}H-NMR- and 2-dimensional rotating frame nuclear Overhauser effect spectroscopy- (EASY ROESY) spectra were recorded with a NMR Ascent 700 spectrometer (700 MHz) equipped with a cryogenic probe with z-gradient at 298 K. The ROESY field strength was 5000 Hz. The magnetization was locked at an angle of 45° off the z-axis which ensures suppression of TOCSY artefacts. Chemical shifts were referenced to residual HDO.[17]

Discussion

In the aqueous $NaHCO_3$/Na_2CO_3 buffer (pH = 10.5, ionic strength $I \approx 0.25$ M), which was used as a solvent, the three azo dyes shown in Fig. 1 are present in their phenolate form in all cases, as the phenolic hydroxyl group common to all dyes is deprotonated. Fig. 2 compares the absorption spectra of all three dyes at a concentration of 5 mM. In the following, a brief overview of UV/vis spectroscopic observations will be given for all three dyes, followed by a detailed discussion of some specifically interesting features.

First insights into dye solubility and self-aggregation can be obtained from UV/vis spectroscopy: in case the dye is soluble on a molecular level and does not self-aggregate, Beer–Lambert

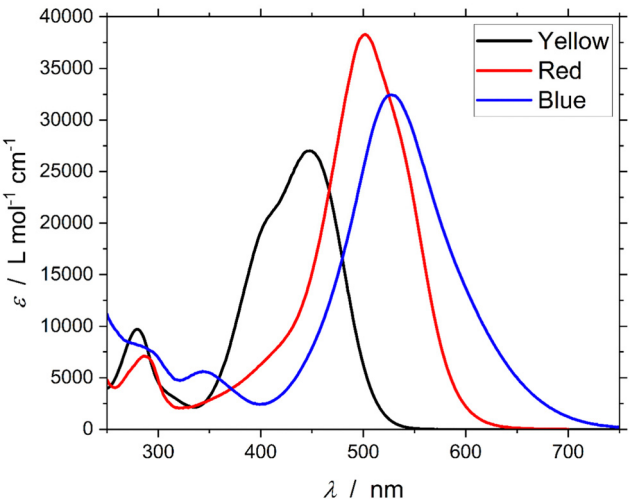

Fig. 2 UV/vis spectra of the three investigated dyes at a concentration of 5 mM and pH = 10.5 in an aqueous $NaHCO_3$/Na_2CO_3 buffer ($I \approx 0.25$ M) at 25 °C. At the given pH all dye molecules are present in their phenolate form.

law (eqn (1)) is fulfilled at each wavelength of the absorption spectrum.

$$A = \log\left(\frac{I_0}{I}\right) = [\mathrm{Dye}]_{\mathrm{tot}} \cdot d \cdot \varepsilon \quad (1)$$

In eqn (1), $[\mathrm{Dye}]_{\mathrm{tot}}$ is the total molar concentration of dye in the sample, d is the optical path length and ε is the molar extinction coefficient. To facilitate discussion, the absorbance divided by optical path length A_{d} will be referred to as "Absorbance".

$$A_{\mathrm{d}} = \frac{A}{d} = [\mathrm{Dye}]_{\mathrm{tot}} \cdot \varepsilon \quad (2)$$

In case the dye does not self-aggregate, A_{d} is expected to linearly increase with $[\mathrm{Dye}]_{\mathrm{tot}}$.[18] For the reported systems this is only the case for the dye Yellow up until its solubility limit of $[\mathrm{Yellow}]_{\mathrm{tot}}$ = 11 mM. Corresponding investigations are displayed in the ESI,† Fig. S1. Dynamic and static light scattering confirm the absence of self-aggregation in solutions of Yellow (Fig. S3 and S4, ESI†). Opposed to Yellow, UV/vis absorption spectra of Blue and Red significantly change with increasing $[\mathrm{Dye}]_{\mathrm{tot}}$. In both cases, the main absorption maximum experiences a blue-shift with increasing concentration of dye, which points towards H-aggregation (face-to-face-aggregation).[12,18,19] Furthermore, a solubility limit as observed for Yellow was not observed for Blue and Red in the investigated concentration range of up to 25 mM (Fig. S1, ESI†). Hence, the observed spectral changes are typical for the formation of soluble aggregates and will be discussed for Blue and Red separately.

Self-assembly of Blue

Concentration-induced changes in the absorption spectrum of Blue were attributed to dimer formation: Fig. 3 shows UV/vis absorption spectra of solutions containing different concentrations of Blue.

Increasing $[\mathrm{Blue}]_{\mathrm{tot}}$ leads to a shift of the absorption maximum to lower wavelengths and a decrease in the maximum molar extinction coefficient $\varepsilon_{\mathrm{max}}$. In addition to that, an isosbestic point at $\lambda_{\mathrm{isosbestic}}$ = (655 ± 2) nm and $\varepsilon_{\mathrm{isosbestic}}$ = (4350 ± 110) L mol^{-1} cm^{-1} is observed. This is characteristic of only two species contributing to the total sample absorption.[12,20] Even though absorption spectra do not directly provide information on aggregation number, it is reasonable to assume an equilibrium between a monomeric dye molecule M and a dimer D.

$$2\ \mathrm{M} \rightleftharpoons \mathrm{D}\quad K_{\mathrm{D}} = \frac{[\mathrm{D}]}{[\mathrm{M}]^2} \quad (3)$$

[M] and [D] are molar equilibrium concentrations of the monomer and the dimer. K_{D} is the dimerization constant. Assuming that both, the monomer and the dimer contribute to the absorbance of the solution, A_{d} can be calculated at each wavelength λ.

$$A_{\mathrm{d}}(\lambda) = [\mathrm{M}] \cdot \varepsilon_{\mathrm{M}}(\lambda) + [\mathrm{D}]\ \varepsilon_{\mathrm{D}}(\lambda) \quad (4)$$

$\varepsilon_{\mathrm{M}}(\lambda)$ and $\varepsilon_{\mathrm{D}}(\lambda)$ are monomer and dimer molar extinction coefficients at wavelength λ. The total molar concentration of Blue $[\mathrm{Blue}]_{\mathrm{tot}}$ is calculated as shown in eqn (5).

$$[\mathrm{Blue}]_{\mathrm{tot}} = [\mathrm{M}] + 2 \cdot [\mathrm{D}] \quad (5)$$

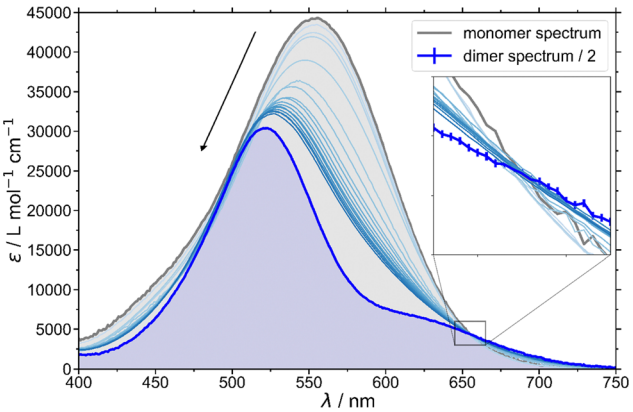

Fig. 3 Spectra of Blue recorded at 25 °C in buffer solution at different concentrations. The arrow indicates an increase in $[\mathrm{Blue}]_{\mathrm{tot}}$ from 0.01 mM to 6 mM. The monomer spectrum was recorded at $[\mathrm{Blue}]_{\mathrm{tot}}$ = 5 μM. The dimer spectrum results from fitting. It was divided by 2 to refer to the concentration of monomer. The inset magnifies the region around the isosbestic point.

Inserting eqn (3) and (5) into (4) permits the calculation of A_{d} from $[\mathrm{Blue}]_{\mathrm{tot}}$ at any given wavelength, once the molar extinction coefficients of monomer and dimer and the dimerization constant K_{D} are known (eqn (6)).[20–22]

$$A_{\mathrm{d}}(\lambda) = \varepsilon_{\mathrm{M}}(\lambda)\left(\frac{-1 \pm \sqrt{1 + 8K_{\mathrm{D}} \cdot [\mathrm{Blue}]_{\mathrm{tot}}}}{4K_{\mathrm{D}}}\right) + \varepsilon_{\mathrm{D}}(\lambda)\left(\frac{[\mathrm{Blue}]_{\mathrm{tot}}}{2} - \frac{-1 \pm \sqrt{1 + 8K_{\mathrm{D}} \cdot [\mathrm{Blue}]_{\mathrm{tot}}}}{8K_{\mathrm{D}}}\right) \quad (6)$$

The molar extinction coefficient of the monomer $\varepsilon_{\mathrm{M}}(\lambda)$ was retrieved from a measurement at a very low concentration of Blue $[\mathrm{Blue}]_{\mathrm{tot}}$ = 5 μM. Eqn (6) was fitted to spectroscopic data $A_{\mathrm{d}}(\lambda) = f([\mathrm{Blue}]_{\mathrm{tot}})$ to obtain the dimer molar extinction coefficient $\varepsilon_{\mathrm{D}}(\lambda)$ for each wavelength. In addition to that, the dimerization constant K_{D} was fitted as a global parameter, independent of the wavelength. The analysis was performed at wavelengths ranging from 400 nm to 750 nm with a resolution of $\Delta\lambda$ = 1 nm. The least squares algorithm implemented in the scipy.optimize.leastsq method of the Python SciPy module was used for the optimization of fit parameters.[23] The source code can be found in the ESI.† From that optimization, a dimerization constant of K_{D} = (728 ± 8) L mol^{-1} was obtained with χ_{red}^2 = 0.35. The dimer spectrum is shown in Fig. 3. In this graph, the dimer molar extinction coefficient was divided by 2 to refer to dye monomer concentration and hence visualize the expected change in sample spectra more clearly.

The dimer spectrum in Fig. 3 shows two clearly discernible peaks with absorption maxima at energies higher and lower than that of the monomer. This can be explained by exciton theory where the first excited energy state of the monomer splits into two due to dipole–dipole interaction in case the transition dipole moments of the two monomers are aligned in a face-to-face mode (H-aggregation).[24] The transition with the

higher energy is based on an in-phase oscillation of the two transition dipole moments and the transition with the lower energy is attributed to an out-of-phase oscillation of the two transition dipole moments.[24] In this context, the change in dye absorption spectrum permits insight into dimer geometry.[19,25] Quantitative analysis of the Blue dimer spectrum was performed and geometrical parameters of the dimer calculated. This calculation and the model are discussed in detail in the ESI.† It was found, that the transition dipole moments of two interacting molecules are twisted by an angle of $\alpha = 42^\circ$. The two transition dipole moments show no inclination, meaning that the centres of two molecules are stacked on top of each other. The interplanar spacing R between those centres was determined to be R = 5.2 Å in the model of non-parallel transition dipoles.

SANS was carried out on two solutions of Blue (Fig. 4). The sample containing $[\text{Blue}]_{\text{tot}}$ = 5 mM shows a lower scattering intensity I_s than the sample with $[\text{Blue}]_{\text{tot}}$ = 10 mM. Furthermore, the scattering intensity declines at higher values of the modulus of the scattering vector q for $[\text{Blue}]_{\text{tot}}$ = 5 mM. These observations point towards a lower mass and smaller size of assemblies in the sample with $[\text{Blue}]_{\text{tot}}$ = 5 mM.

Guinier analysis was performed to obtain forward scattering intensities I_0 and the average radius of gyration of the scatterers R_g according to eqn (7).[26]

$$\ln(I_s) = \ln(I_0) - \frac{R_g^2}{3} \cdot q \tag{7}$$

R_g obtained for both samples are summarized in Table 1. Linearized Guinier plots can be found in the ESI† (Fig. SI8). From I_0 the coherent forward scattering intensity $I_{0,\text{coherent}}$ is obtained by subtracting the incoherent background $BG_{\text{in coherent}}$. The value for the incoherent background was determined by averaging I_s in the high-q range of the scattering curve which is displayed as dashed line in Fig. 4. The weight-averaged molar mass of the scatterers M_w can then be determined from $I_{0,\text{coherent}}$ with eqn (8).[16]

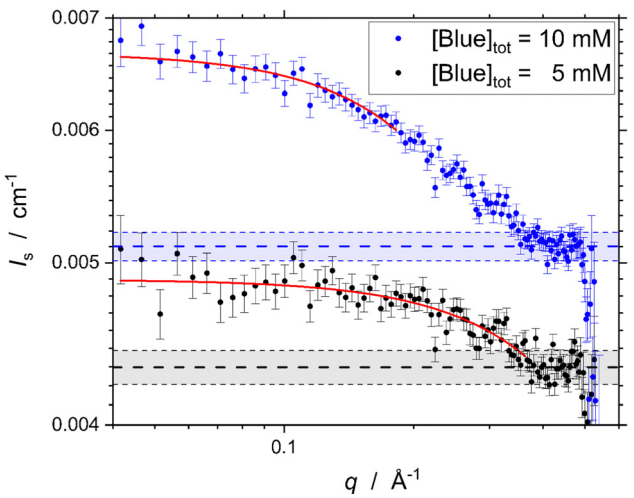

Fig. 4 SANS curves of two solutions of Blue and corresponding Guinier analysis (red lines). The incoherent background is displayed as dashed line with its error indicated as the light-blue or light-grey region.

Table 1 Parameters for absolute analysis of SANS forward scattering intensity of Blue solutions and comparison to calculations from known dimerization constant

Parameter	$[\text{Blue}]_{\text{tot}}$ = 5 mM	$[\text{Blue}]_{\text{tot}}$ = 10 mM
c [10^{-3} g cm^{-3}]	1.85 ± 0.02	3.70 ± 0.03
ρ_s [cm^{-2}]	3.004×10^{10}	
ρ_{solv} [cm^{-2}]	6.376×10^{10}	
$V_{m,s}$ [cm^3 mol^{-1}]	246.31	
M_s [g mol^{-1}]	368.82	
SANS	$[\text{Blue}]_{\text{tot}}$ = 5 mM	$[\text{Blue}]_{\text{tot}}$ = 10 mM
$I_{0,\text{coherent}}$ [10^{-3} cm^{-1}]	0.6 ± 0.1	1.6 ± 0.1
M_w [g mol^{-1}]	362 ± 97	502 ± 47
R_g [Å]	1.6 ± 0.1	3.1 ± 0.1
K_D = (728) L mol^{-1}	$[\text{Blue}]_{\text{tot}}$ = 5 mM	$[\text{Blue}]_{\text{tot}}$ = 10 mM
[M] [mM]	1.54 ± 0.02	2.30 ± 0.02
[D] [mM]	1.73 ± 0.01	3.85 ± 0.01
M_w (K_D) [g mol^{-1}]	624 ± 1	653 ± 1

$$I_{0,\text{coherent}} = I_0 - BG_{\text{in coherent}} = c \cdot K \cdot M_w \tag{8}$$

$$K\left[\frac{\text{cm}^2\,\text{mol}}{\text{g}^2}\right] = \frac{(\rho_s - \rho_{\text{solv}})^2 \cdot V_{m,s}^2}{M_s^2 \cdot N_A} \tag{9}$$

c is the mass concentration of the solute Blue, ρ_s and ρ_{solv} the scattering length densities of the elementary scattering units of solute and solvent respectively, $V_{m,s}$ is the molar volume of the elementary scattering unit of the solute and M_S its molar mass. N_A is Avogadro's number. These parameters and results from analysis of absolute forward scattering intensities are summarized in Table 1.

The weight average molar mass of the scatterer is furthermore compared to the theoretical weight average molar mass of a mixture of Blue monomers and dimers according to the dimerization equilibrium described by eqn (3) with the calculated dimerization constant of K_D = (728 ± 8) L mol^{-1}. Knowing the total molar dye concentration, the molar concentrations of Blue monomer [M] and Blue dimer [D] are obtained by combining eqn (3) and (5). $M_w(K_D)$ is then obtained from:

$$M_w(K_D) = \frac{[\text{M}] \cdot M_s^2 + [\text{D}] \cdot (2M_s)^2}{[\text{M}] \cdot M_s + [\text{D}] \cdot 2M_s} \tag{10}$$

As the elementary scattering unit corresponds to one Blue molecule, M_s is the molar mass of Blue.

From Table 1, several observations are made: (1) according to Guinier analysis, M_w and R_g of scatterers in the sample containing $[\text{Blue}]_{\text{tot}}$ = 10 mM are higher than M_w and R_g of scatterers in the sample containing $[\text{Blue}]_{\text{tot}}$ = 5 mM. This is consistent with the assumption of concentration-induced aggregation. (2) Due to the extremely low scattering intensities from the dye solutions and concomitant poor statistics, errors in M_w from SANS are high in this case. (3) M_w from SANS does not directly compare to $M_w(K_D)$ from the experiments presented here. This could be due to the high error in M_w, low values of M_w and uncertainty in scattering contrast.[27] It should, however, be noted that M_w from SANS is smaller than $M_w(K_D)$ in both cases, rendering the possibility of aggregates of more than two

monomers unlikely. (4) The radius of gyration of the scatterers at either concentration is very small. Considering the model of a homogeneous cylinder, R_g = 4 Å was estimated for the dimer considering its chemical structure and results from exciton analysis. The calculation is outlined in the ESI.† R_g = 4 Å is not significantly higher than the experimentally determined R_g from SANS for the sample with $[Blue]_{tot}$ = 10 mM. A direct comparison of this theoretical value to the experimental ones is difficult, as each solution contains a mixture of monomer and dimer and the homogeneous cylinder model is only an approximation. Nevertheless it shows that the interplanar spacing R = 5.2 Å obtained by exciton theory is within an acceptable size range.

Information on the cause for dimer formation in solutions of Blue may be obtained by elucidating how Blue molecules assemble within the dimeric aggregate. For this purpose, ROESY (rotating frame nuclear Overhauser effect spectroscopy) has been used to evaluate correlations through space. This type of NOE (nuclear Overhauser effect) spectroscopy permits to study the spatial proximity of protons up to a distance of about 5 Å.[28] In contrast to the more frequently performed NOESY (nuclear Overhauser effect spectroscopy), ROESY cross peak signals are always positive and do not vanish if the molecule or assembly exhibits a medium tumbling rate.[29,30] Fig. 5 displays the ROESY spectrum of a solution containing $[Blue]_{tot}$ = 10 mM. Cross peaks for signals a'–b' and d'–e' are expected due to the chemical structure of Blue. However, cross peaks are also observed between signals a'–e', b'–f' and c'–f'. They exhibit much weaker intensities than the cross peaks mentioned before, which is likely caused by a greater distance between corresponding protons. These cross peaks are therefore related to the proximity of protons of two different molecules.

Fig. 6(B) displays the structure of the Blue dimer, which explains cross peaks that were observed in the ROESY spectrum and is chemically meaningful. For readability, observed intermolecular NOE couplings are marked on two aligned but displaced chemical structures of Blue in Fig. 6(A). In terms of intermolecular interactions, three major driving forces leading

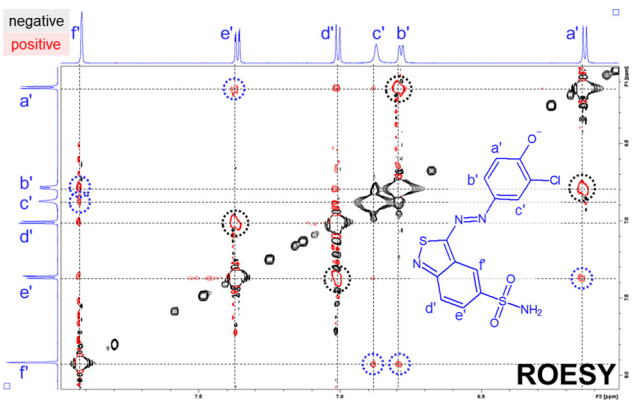

Fig. 5 ROESY spectrum of a solution containing $[Blue]_{tot}$ = 10 mM in a $NaHCO_3/Na_2CO_3$ buffer with pD = 10.7 and $I \approx$ 0.25 M prepared in D_2O. Cross-peaks arising due to the proximity of protons as expected by chemical structure are encircled in black. Cross peaks arising due to intermolecular proximity of protons are encircled in Blue.

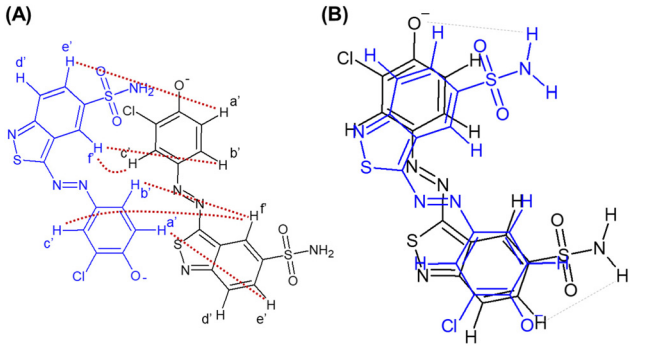

Fig. 6 Fig. 6 (A) Chemical structure of two molecules of Blue aligned as expected in the dimeric assembly but displaced for visibility. Protons are labelled according to the peak assignment in the ROESY spectrum (Fig. 5). Observed intermolecular NOE coupling is indicated by red dotted lines. (B) Structure of the Blue dimer. Grey, dotted lines indicate potential hydrogen bonding interactions.

to the observed self-assembly are expected: (1) electrostatic repulsion between negatively charged phenolate groups, (2) π–π stacking of aromatic moieties and (3) hydrogen bonding interactions between the phenolate oxygen atom and hydrogen atoms from the sulphonamide groups.

The formation of assemblies with higher aggregation numbers may be hindered by steric requirements of the sulphonamide group and resulting packing constraints as well as electrostatic repulsion between nearby phenolate groups, which supports the assumption of dimer formation.

The dimer structure shown in Fig. 6(B) is relatively symmetrical, indicating that protons from both molecules participating in dimer formation experience similar chemical environments, which leads to narrow ^{1}H-NMR signals.[28] Furthermore, the proposed structure complies with results from preceding analysis of UV/vis spectra according to exciton theory: within the model of non-planar transition dipoles a tilt angle α = 42° between two molecular planes was found, which agrees with the proposed structure as these planes are not given a direction and $\alpha < 90°$.[19] Furthermore, an interplanar spacing of R = 5.2 Å does not rule out the occurrence of a NOE between interacting Blue molecules.

To conclude this section, the self-assembly of Blue in an aqueous $NaHCO_3/Na_2CO_3$ buffer with pH = 10.5 and $I \approx$ 0.25 M was elucidated using UV/vis-spectroscopy, SANS and NMR-spectroscopy. Concentration-dependent UV/vis spectra pointed towards dimer formation and H-aggregation of Blue molecules with a dimerization constant of K_D = (728 ± 8) L mol^{-1}. SANS confirmed concentration-induced aggregation while proving higher-than-dimer aggregation unlikely. Dimer geometry was elucidated with the help of NMR-spectroscopy and the quantitative analysis of UV/vis spectra according to exciton theory, suggesting π–π- and hydrogen bonding interactions as the most relevant attractive forces. Conversely, electrostatic repulsion between phenolate groups and steric requirements of the sulphonamide group potentially inhibit the formation of higher-order aggregates.

Self-assembly of Red

The absorption spectra of the dye Red are affected by concentration induced self-aggregation (Fig. 7). An increase in

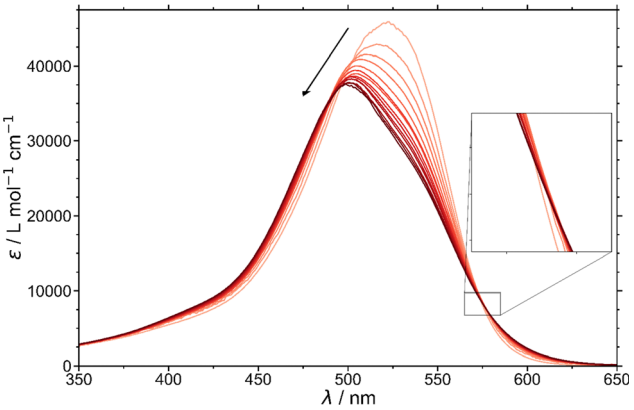

Fig. 7 Spectra of Red recorded at 25 °C in buffer solution at different concentrations. The arrow indicates an increase in $[Red]_{tot}$ from 0.002 mM to 6 mM. The inset shows a region where an isosbestic point could be assumed but does not exist.

concentration leads to a shift of the absorption maximum to lower wavelengths. However, no well-defined isosbestic point exists, suggesting more than two absorbing species contributing to the overall spectrum. Therefore, we abstained from an attempt to decompose the spectra into contributions from components.

SANS was performed on solutions of Red (Fig. 8), one solution containing $[Red]_{tot}$ = 10 mM and the other one containing Red at an approximate concentration of $[Red]_{tot} \approx 5$ mM. The concentration of Red in the latter sample was obtained by comparing forward scattering intensities of both SANS curves, as the sample with $[Red]_{tot} \approx 5$ mM was intended to contain a higher concentration of Red, but was filtered too soon after its preparation when the dye was not yet completely dissolved, resulting into a loss of material. Details can be found in the ESI† (Fig. S10). For both curves, two Guinier shoulders are discernible at $q < 0.003$ Å^{-1} and $q > 0.05$ Å^{-1}. This likely results from scattering of at least two morphological features: A small structure, showing a Guinier-plateau in the high-q region

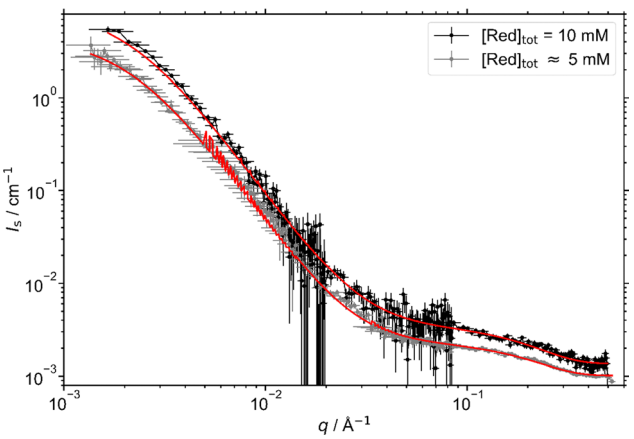

Fig. 8 SANS data of two solutions of Red in buffer and at 25°. The form factor fit corresponding to the contribution of a Guinier fit (R_g = 8.5 Å) with a fractal structure ($D_f = 2.66 \pm 0.03$, $L_{corr} = (437 \pm 10)$ Å, $R_{block} = (9 \pm 1)$ Å) is shown as a red line.[31] Both displayed fits only differ by scaling factors. $\chi^2([Red]_{tot}$ = 10 mM) = 1.52, $\chi^2([Red]_{tot} \approx 5$ mM) = 3.31.

at $q > 0.05$ Å^{-1} and a large structure, causing the scattering intensity in the mid- and low-q region to rise.

The radius of gyration of the species contributing to the scattering signal in the high-q region was determined to 8.5 Å by model-independent Guinier analysis for both curves. Furthermore, the SANS curves were described using the sum of a fractal form factor and a Guinier fit.[31] The fractal model describes the mid- and low-q region and is characterized by the radius of spherical building blocks, R_{block}, its scattering length density ρ_{block}, the fractal dimension D_f and the cluster correlation length L_{corr}, which represents the total fractal cluster size. $R_{block} = (9 \pm 1)$ Å was found to be similar to R_g = 8.5 Å obtained for the small species. The sum of a fractal model and a Guinier fit describes both SANS curves sufficiently well. Both curves can be described using identical geometrical parameters and fractal dimension when permitting the scaling of the fractal and the Guinier contribution to be different. Size parameters are given in the caption of Fig. 8 and are summarized in the ESI† (Table S2).

Aside from reproducing the scattering pattern of true fractals, the fractal form factor model can often be used for hierarchically structured aggregates, which cannot be further specified in terms of a more specific form factor model such as sphere, ellipsoid or cylinder without introducing a large number of fitting parameters, *e.g.* concerning polydispersity.[32–34] The fractal model has been successfully applied for instance in asphaltene research, where asphaltene molecules in a nonpolar solvent are assumed to aggregate in a three-step hierarchy from core aggregates due to π–π-stacking of molecules, over medium aggregates, which are secondary aggregates of core aggregates, to fractal aggregates.[35]

Concerning the dye Red, the assumption of π–π-stacking interactions leads to cylinders as the first choice to describe SANS curves of corresponding solutions.[4] However, an apparent scaling of $I_s \propto q^{-2.66}$ instead of $I_s \propto q^{-1}$ in the low- to mid-q region contradicts the presence of simple, non-interacting cylinders.[36] Furthermore, the Kratky plot of corresponding SANS curves (Fig. S11, ESI†) shows an initial maximum and in the Holtzer plot (Fig. S12, ESI†) a minimum is visible before reaching a plateau in the high-q region. Both observations point towards a structure, which is more compact than a random coil polymer chain.[36] However, these observations do not rule out the existence of cylinders as a structural feature, particularly because a $I_s \propto q^{-1}$ dependency is observed in the mid- to high-q region. A possible explanation could be branching of these cylinders.[37,38] A more in-depth discussion is given in the ESI.† The presence of at least two structural levels is therefore likely to occur and visualized in Fig. 9. Herein, the formation of cylinder-like aggregates induced by π–π-stacking of Red is the onset of the aggregation. These π-stacks may elongate to cylindrical aggregates, which could show branching. Alternatively, further assembly of short cylinder segments may lead to fractal aggregates. The cluster correlation length in the fractal model would correspond to the overall size of the branched cylinder aggregate and the thickness (or size) of the building units in the fractal model would reproduce the cylinder cross section in the branched cylinder picture.

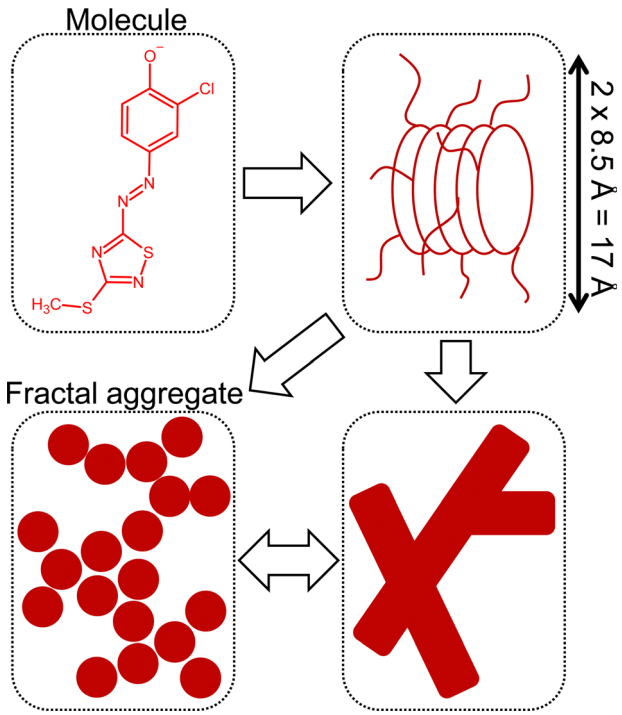

Fig. 9 Potential hierarchy in the aggregation of Red. The image and theory were adapted from considerations regarding the aggregation of asphaltenes in *n*-heptane according to Tanaka *et al.*[35]

Fig. 10 shows the ^{1}H-NMR spectrum of a 10 mM solution of Red. In addition to that, it was attempted to obtain an idea about spatial proximity of protons belonging to different Red molecules using ROESY (Fig. S15, ESI†). However, no cross peaks were observed in the ROESY spectrum. As not even the *a*–*b* cross peak expected from chemical structure of the Red molecule was visible, the absence of observable spatial correlations in the ROESY spectrum was attributed to the extreme peak broadening of signals *b* and *c*. Peak broadening is often a sign of aggregation arising from increased spin–spin relaxation rates due to slower molecular motion in aggregates.[39,40] This is a rather frequently observed phenomenon for systems exhibiting π–π-stacking, like dye molecules in solution.[30,41,42] Nevertheless it is remarkable, that signals *a* and *d* are not as strongly line broadened as signals *b* and *c*, which could result from corresponding protons experiencing a smaller variety of chemical environments and protons of type *d* potentially tumbling faster leading to the observation of an average chemical shift.[43] Following these observations, protons b and c are likely located closer to the structural sub-unit leading to intermolecular aggregation of Red, which results in a greater variety of chemical environments and rigidity, whereas protons of type *a* and *d* are located further away from that part of the molecule. Considering that π–π-stacking interactions between 1,2,4-oxadiazole moieties were shown of great relevance for the aggregation of molecules containing such a heterocycle, it is likely that the aggregation of Red molecules results from π–π-stacking interactions between the similar 1,2,4-thiadiazole heterocyclic moieties.[44] This aligns well with the assumption of electrostatic repulsion between phenolate groups, as these are free to point towards opposite directions when π–π-stacking occurs on the 1,2,4-thiadiazole aromatic sub-unit.

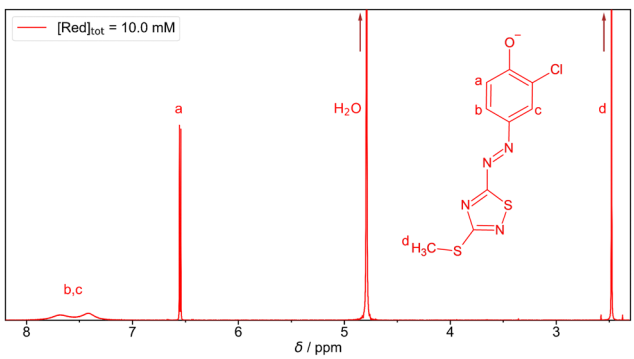

Fig. 10 ^{1}H-NMR spectrum of a solution containing Red at $[Red]_{tot}$ = 10 mM in a $NaHCO_3/Na_2CO_3$ buffer (pD = 10.7, $I \approx 0.25$ M) prepared in D_2O.

To conclude, the self-assembly of Red in an aqueous $NaHCO_3/Na_2CO_3$ buffer with pH = 10.5 and $I \approx 0.25$ M commences with a cylindrical arrangement of Red monomers. NMR spectroscopic investigations suggest π–π-stacking between the 1,2,4-thiadiazole sub-units of different Red molecules to be the main reason for this arrangement. The cylinders probably elongate and eventually branch. The SANS curves of the resulting aggregates can be reproduced by a simplified fractal model.

Conclusions

Three 3-chloro-4-hydroxy-phenylazo dyes, each of them carrying a negative charge due to deprotonation of the phenolic hydroxyl group at alkaline pH, were shown to significantly differ in their self-assembly behaviour. This confirms the complexity of intermolecular interactions and the difficulty to predict assembly behaviour of molecules just from their chemical structure.

Unlike to Blue and Red, the dye Yellow does not self-assemble. In addition to that, Yellow shows a solubility limit of 11 mM in the aqueous buffer used as a solvent, which was not observed for the other dyes. The lack of Yellow self-aggregation can be attributed to the impossibility to form intermolecular π–π-stacking interactions. π–π-stacking between phenolate groups is likely hindered by electrostatic repulsion between the deprotonated hydroxyl groups. Furthermore, π–π-stacking between pyrazole sub-units might be hindered by steric constraints due to the substitution of one nitrogen atom with a methyl group.

The self-assembly of Blue and Red can be followed using UV/vis spectroscopy. Blue was observed to form dimers with a dimerization constant of $K_D = (728 \pm 8)$ L mol^{-1}. With the calculated dimer spectrum, H-aggregation of Blue molecules is revealed. Their aggregation geometry calculated with exciton theory, yields a twist angle of transition dipole moments of $\alpha = 42^\circ$ and an interplanar spacing of 5.2 Å in the model of non-parallel transition dipoles. Driving forces for self-aggregation include π–π-stacking, electrostatic repulsion between phenolate groups and likely hydrogen bonding between the phenolate

oxygen and hydrogen atoms of the sulphonamide group. Steric effects due to spatial requirements of the sulphonamide group and electrostatic repulsion between phenolate groups pointing towards the same direction could hinder the formation of larger aggregates.

The self-aggregation of Red is more complex than that of Blue. The absence of an isosbestic point in concentration-dependent UV/vis spectra suggests the presence of multiple aggregate species. SANS revealed an average aggregate size of at least 400 Å. Self-aggregation of Red likely occurs due to π–π-stacking of the 1,2,4-thiadiazole sub-unit, leading to cylindrical building blocks which are able to form larger aggregate structures, most likely *via* branching.

Following these investigations, it becomes evident, that assembly properties cannot easily be predicted based on structural similarities. Rather, assembly morphology is directed by a subtle balance of intermolecular interactions and steric effects, which can be influenced dramatically by minor constitutional changes. Therefore, care has to be taken when expecting similar behaviour from molecules with similar chemical functionalities.

Author contributions

Conceptualization: WM, RS, BN, KH, experimental: WM, RS, HE, analysis: WM with contributions from RS, HE, KH, BN, writing: WM, editing: WM, RS, BN, KH, HE, funding acquisition: RS, BN, KH.

Conflicts of interest

There are no conflicts to declare.

Acknowledgements

The authors thank the Institut Laue-Langevin for the provision of internal beamtime (**https://doi.ill.fr/10.5291/ILL-DATA.INTER-557**). The authors gratefully acknowledge the use of the Partnership for Soft Condensed Matter (PSCM) facilities. W. M. acknowledges funding for a PhD scholarship from the European Union's Horizon 2020 research and innovation programme under the Marie Skłodowska-Curie grant agreement No 847439 within the InnovaXN framework (Project number XN2019-ILL23).

Notes and references

1 T. Bechtold, A. Mahmud-Ali and R. Mussak, *Dyes Pigm.*, 2007, **75**, 287–293.
2 N. ElGuesmi, A. Farghaly, A. Y. Khormi, M. R. Shaaban, K. P. Katin and S. Kaya, *J. Mol. Struct.*, 2023, **1271**, 134002.
3 H. Jiang, L. Zhang, J. Cai, J. Ren, Z. Cui and W. Chen, *Dyes Pigm.*, 2018, **151**, 363–371.
4 D. Bialas, E. Kirchner, M. I. S. Röhr and F. Würthner, *J. Am. Chem. Soc.*, 2021, **143**, 4500–4518.
5 A. Hagfeldt, G. Boschloo, L. Sun, L. Kloo and H. Pettersson, *Chem. Rev.*, 2010, **110**, 6595–6663.
6 P.-T. Chou and Y. Chi, *Chem. – Eur. J.*, 2007, **13**, 380–395.
7 F. Würthner, C. R. Saha-Möller, B. Fimmel, S. Ogi, P. Leowanawat and D. Schmidt, *Chem. Rev.*, 2016, **116**, 962–1052.
8 X. Hu, T. Ritz, A. Damjanović, F. Autenrieth and K. Schulten, *Q. Rev. Biophys.*, 2002, **35**, 1–62.
9 X. Hu, A. Damjanović, T. Ritz and K. Schulten, *Proc. Natl. Acad. Sci. U. S. A.*, 1998, **95**, 5935–5941.
10 H. Tamiaki, *Coord. Chem. Rev.*, 1996, **148**, 183–197.
11 T. S. Balaban, H. Tamiaki and A. R. Holzwarth, in *Supermolecular Dye Chemistry*, ed. F. Würthner, Springer, Berlin, Heidelberg, 2005, pp. 1–38.
12 Z. Chen, A. Lohr, C. R. Saha-Möller and F. Würthner, *Chem. Soc. Rev.*, 2009, **38**, 564–584.
13 C. F. J. Faul and M. Antonietti, *Adv. Mater.*, 2003, **15**, 673–683.
14 Mantid Project, Mantid (2013): Manipulation and Analysis Toolkit for Instrument Data, DOI: **10.5286/SOFTWARE/MANTID**.
15 O. Arnold, J. C. Bilheux, J. M. Borreguero, A. Buts, S. I. Campbell, L. Chapon, M. Doucet, N. Draper, R. Ferraz Leal, M. A. Gigg, V. E. Lynch, A. Markvardsen, D. J. Mikkelson, R. L. Mikkelson, R. Miller, K. Palmen, P. Parker, G. Passos, T. G. Perring, P. F. Peterson, S. Ren, M. A. Reuter, A. T. Savici, J. W. Taylor, R. J. Taylor, R. Tolchenov, W. Zhou and J. Zikovsky, *Nucl. Instrum. Methods Phys. Res., Sect. A*, 2014, **764**, 156–166.
16 *Neutrons, X-rays, and light: scattering methods applied to soft condensed matter*, ed. P. Lindner and T. Zemb, Elsevier, Amsterdam, Boston, 1st edn, 2002.
17 H. E. Gottlieb, V. Kotlyar and A. Nudelman, *J. Org. Chem.*, 1997, **62**, 7512–7515.
18 F. Cuétara-Guadarrama, M. Vonlanthen, K. Sorroza-Martínez, I. González-Méndez and E. Rivera, *Dyes Pigm.*, 2021, **194**, 109551.
19 M. Kasha, H. R. Rawls and M. A. El-Bayoumi, *Pure Appl. Chem.*, 1965, **11**, 371–392.
20 B. Neumann, K. Huber and P. Pollmann, *Phys. Chem. Chem. Phys.*, 2000, **2**, 3687–3695.
21 M.-L. Horng and E. L. Quitevis, *J. Chem. Educ.*, 2000, **77**, 637.
22 R. Sabaté, M. Gallardo, A. de la Maza and J. Estelrich, *Langmuir*, 2001, **17**, 6433–6437.
23 P. Virtanen, R. Gommers, T. E. Oliphant, M. Haberland, T. Reddy, D. Cournapeau, E. Burovski, P. Peterson, W. Weckesser, J. Bright, S. J. van der Walt, M. Brett, J. Wilson, K. J. Millman, N. Mayorov, A. R. J. Nelson, E. Jones, R. Kern, E. Larson, C. J. Carey, İ. Polat, Y. Feng, E. W. Moore, J. VanderPlas, D. Laxalde, J. Perktold, R. Cimrman, I. Henriksen, E. A. Quintero, C. R. Harris, A. M. Archibald, A. H. Ribeiro, F. Pedregosa and P. Van Mulbregt, *Nat. Methods*, 2020, **17**, 261–272.
24 M. Kasha, *Radiat. Res.*, 1963, **20**, 55–70.
25 K. K. Rohatgi, *J. Mol. Spectrosc.*, 1968, **27**, 545–548.
26 W. Schärtl, *Light Scattering from Polymer Solutions and Nanoparticle Dispersions*, Springer Berlin Heidelberg, Berlin, Heidelberg, 2007.
27 K. A. Rubinson, C. Stanley and S. Krueger, *J. Appl. Crystallogr.*, 2008, **41**, 456–465.

28 J. B. Lambert, *Spektroskopie: Strukturaufklärung in der Organischen Chemie*, Pearson, 2012.
29 T. D. W. Claridge, *High-Resolution NMR Techniques in Organic Chemistry*, Elsevier, 2nd edn, 2009, vol. 27, pp. 247–302.
30 M. P. Renshaw and I. J. Day, *J. Phys. Chem. B*, 2010, **114**, 10032–10038.
31 J. Teixeira, *J. Appl. Crystallogr.*, 1988, **21**, 781–785.
32 M. P. Hoepfner, C. Vilas Bôas Fávero, N. Haji-Akbari and H. S. Fogler, *Langmuir*, 2013, **29**, 8799–8808.
33 J. Eyssautier, P. Levitz, D. Espinat, J. Jestin, J. Gummel, I. Grillo and L. Barré, *J. Phys. Chem. B*, 2011, **115**, 6827–6837.
34 K. L. Gawrys, G. A. Blankenship and P. K. Kilpatrick, *Langmuir*, 2006, **22**, 4487–4497.
35 R. Tanaka, E. Sato, J. E. Hunt, R. E. Winans, S. Sato and T. Takanohashi, *Energy Fuels*, 2004, **18**, 1118–1125.
36 J. S. Pedersen, *Adv. Colloid Interface Sci.*, 1997, **70**, 171–210.
37 K. Huber and W. Burchard, *Macromolecules*, 1989, **22**, 3332–3336.
38 K. Huber, W. Burchard, S. Bantle and L. J. Fetters, *Polymer*, 1987, **28**, 1997–2003.
39 D. J. Edwards, J. W. Jones, O. Lozman, A. P. Ormerod, M. Sintyureva and G. J. T. Tiddy, *J. Phys. Chem. B*, 2008, **112**, 14628–14636.
40 C. Shao, M. Grüne, M. Stolte and F. Würthner, *Chem. – Eur. J.*, 2012, **18**, 13665–13677.
41 M. J. Ahrens, L. E. Sinks, B. Rybtchinski, W. Liu, B. A. Jones, J. M. Giaimo, A. V. Gusev, A. J. Goshe, D. M. Tiede and M. R. Wasielewski, *J. Am. Chem. Soc.*, 2004, **126**, 8284–8294.
42 M. J. Ahrens, R. F. Kelley, Z. E. X. Dance and M. R. Wasielewski, *Phys. Chem. Chem. Phys.*, 2007, **9**, 1469–1478.
43 I. Furó, *J. Mol. Liq.*, 2005, **117**, 117–137.
44 S. V. Baykov, A. S. Mikherdov, A. S. Novikov, K. K. Geyl, M. V. Tarasenko, M. A. Gureev and V. P. Boyarskiy, *Molecules*, 2021, **26**, 5672.